Flexural behaviour of timber dovetail mortise-tenon joints

Flexural behaviour of timber dovetail mortise-tenon joints

Chunchao Chen [a], Hongxing Qiu [a,*], Yong Lu [b]

[a] Key Laboratory of Concrete and Prestressed Concrete Structures of Ministry of Education, Southeast University, Nanjing 210096, China

[b] Institute for Infrastructure and Environment, School of Engineering, The University of Edinburgh, Edinburgh EH9 3JL, UK

([*]Corresponding author. E-mail: qiuhx@seu.edu.cn)

Abstract: A comprehensive study has been carried out on the flexural behaviour of dovetail mortise-tenon joints in timber structures. Two types of the joints have been considered; type 1 represents a joint at the top of a column where the beam tenon may be slid into the mortise from above the column, and type 2 represents a joint below the top of a column where the beam tenon needs to be inserted from the side into the mortise. Relationships of moment vs. rotation and tenon pull-out vs. rotation, as well as the failure modes were obtained from experiments under monotonic loading. Numerical simulation was conducted to examine the deformation states and the stress distributions. On the basis of the experimental and numerical data, a simplified mechanics model has been proposed for the analysis of the moment vs. rotation relationship. Results show that the main failure mode of the dovetail joints is pull-out, and due to the dovetail shape on the two sides of the tenon, the side gaps tend to have a more significant effect than the gaps at the top and the apex. The moment-rotation relationship of the joints has an initial stage of gradual development of nonlinearity, followed by a prolonged yielding phase, and then a descending branch. The moment-rotation relationship may thus be approximated by a trilinear model. Simplified formulas for determining the key points on the moment-rotation relationship have been shown to agree well with the experimental results.

Key words: dovetail mortise-tenon joints; flexural behaviour; moment-rotation relationship; failure modes; numerical simulation; simplified mechanics model

1 Introduction

Timber structures have been the traditional type of buildings in China, Japan, Korea and many other countries for thousands of years. In China, most existing ancient structures are timber structures or timber-brick composite structures. Research on Chinese ancient timber

structures started from the 19th century [1-2], but most of the early work was about the structural layout, process and history of buildings. In more recent years scholars all over the world have done much more specific research on ancient timber structures with the method of modern mechanics.

Dovetail mortise-tenon joints connecting beams with columns are widely seen in ancient timber structures [3]. The origin of this joining method is not exactly known, but it was already common in ancient timber structures built in Ming and Qing dynasties in China [4]. The load-deformation behaviour of dovetail joints is very complex, and their rotational stiffness and strength plays an important role in the lateral stiffness, integrity and stability of the whole structure. But in general their strength is lower than that of the adjoining beams and columns. An appropriate analysis of the mechanical properties of the dovetail joints is therefore crucial for a reliable evaluation of the safety of a timber structure.

The behaviour of joints in timber structures has been a subject of some extensive studies both experimentally and analytically. However, as generally recognised [5], the mechanical behaviour of timber joints varies among different practices. Some of the studies on various types of the timber joints are briefly summarised below. The joint rotational stiffness has been a focus of many of these studies.

Chang et al [5-6] studied the behaviour of continuous and butted Nuki joints with a special interest in the rotational performance of the joints. An initial gap was considered in the joints. Theoretical models were developed to predict the rotational stiffness of both types of joints with gaps.

King et al. [7] conducted experiments on a kind of commonly used beam-to-column connections, with a tenon in the beam and a mortise in the column. They compared prototype and damaged (with material degradation) joints, and developed a three-parameter semi-rigid connection model for the stiffness of the joints.

D'Ayala and Tsai [8] conducted both experimental and numerical studies of the seismic behaviour of timber joints in a special type of timber structures called "Dieh–Dou" in Taiwan. It was also observed that the stiffness of the timber joints played a significant role in determining the overall displacement of the structure.

Chang and Hsu [9] studied the hysteretic behaviour of traditional Go-Dou and stepped dovetail connections, which are usually used to connect frames together and provide out-of-plane stiffness to timber frames. The prediction models for rotational stiffness and the ultimate moment capacity of these two types of joints were established based upon a statistical approach.

Regarding the specific behaviour of dovetail joints, Chun et al. [10] and Yue [11] conducted many experiments to study the flexural behaviour of dovetail joints and derived empirical skeleton curves. Li et al. [12] introduced various assumptions about the failure modes of dovetail joints and subsequently derived the capacity formulas respectively. The failure rotation limits were not provided. Xu et al. [13] developed a moment-rotation relationship of dovetail joints from the perspective of microcosmic relationship of stress-strain, but the formula was very complex and some important parameters needed to be obtained empirically by regression from experimental data. Pang et al. [14] investigated the influence of beam shoulder on the moment-carrying capacity of dovetail mortise-tenon joints by static loading tests. The moment resistance and the failure mode indicated that the beam shoulder significantly affected the performance of the joints. Seo [15] conducted static and cyclic lateral load tests on two Korean ancient timber frames without vertical load. The frames used dovetail joints to connect beams with columns at the column top. The failure modes of the frames were shear failure or bending failure of mortise branches. Despite these studies, however, theoretical research about dovetail joints is still limited.

This paper presents a comprehensive experimental and analytical study on the flexural behaviour of dovetail mortise-tenon joints for beam-column connections. Two types of the joints are considered, representing respectively two different arrangements of the joint positions. Beam-column joint assemblies have been tested to failure under monotonic loading. To assist in the examination of the local stress and deformation distribution in the mortise and tenon, a finite element model has been developed to simulate the joint assembly with details of the mortise and tenon connections. Based on the experiment and numerical simulation, a set of simplification assumptions have been devised with regard to the stress and deformation patterns. Subsequently, a simplified mechanics model has been developed for the analysis of bending moment-rotation relationship of dovetail mortise-tenon joints.

2 Experiment study

2.1 Configurations of the joints

Two types of dovetail joints are considered in the present study, as shown schematically in Figure 1. The first type (Type 1) has a traditional configuration and the joint is located at the top of the column. The second type (Type 2) is an extended version where the joint is located below the column top.

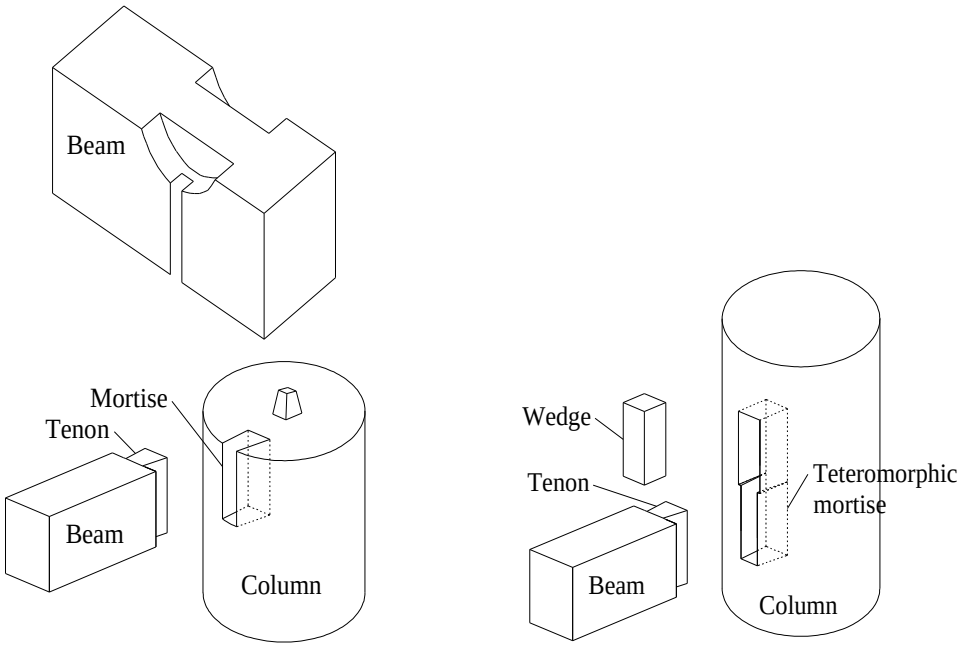

(a) Type 1 joint (located right at top of column) (b) Type 2 joint (located below top of column)

Figure 1 Configurations of the dovetail joints

Because of the dovetail shape of the tenon (the tenon apex is wider than the neck), the tenon cannot be inserted into the mortise directly, so Type 1 configuration has an advantage in that the tenon can be slotted into position vertically from above the mortise. When any other component is subsequently installed on top of the column, such a component will help to hold down the tenon and thus increase the resistance against the rotation of the tenon; otherwise a fixing cap may be required to enable a similar effect.

Type 2 configuration permits a self-contained fixity. The dovetail tenon cannot be inserted directly into the joint in this case, and a wider opening slot needs to be created above the actual mortise to facilitate the installation of the tenon. This effectively renders the mortise to consist of two parts; a wider upper part of right rectangular shape whose width is just enough to allow the passage of the tenon apex, and a dovetail-shaped lower part in which the tenon finally fits. Thus the process of installing the tenon is to firstly bring the tenon into the vertical position through the upper part of the mortise, and then move it down into the lower part of the mortise. Finally a wedge is hammered into the upper part to complete the installation.

2.1 Test specimens

The prototype of the test specimens was made to follow the building practice

documented as from Qing Dynasty. Four 1:1.76 reduced-scale specimens were constructed, and these specimens were designated as JA-1, JA-2, JB-1 and JB-2, respectively. Specimens JA-1 and JA-2 were identical Type-1 joints, and specimens JB-1 and JB-2 were identical Type-2 joints. Detailed dimensions of these specimens are shown in Figure 2. For JA-1 and JA-2, a cap unit was installed on the top of the column to simulate the holding effect from another joining beam. Specimens JB-1 and JB-2 followed the installation procedure described in the previous section.

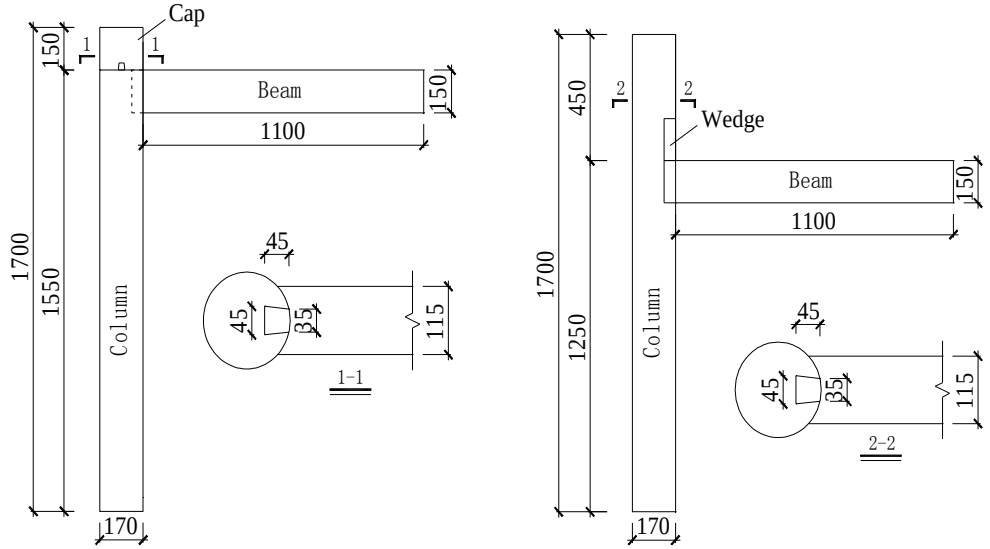

(a) JA-1 and JA-2 (b) JB-1 and JB-2

Figure 2 Dimensions of the specimens (unit: mm)

Table 1 Measured material properties

Elastic constants	$E_{c,R}$ (N/mm^2)	$E_{c,T}$ (N/mm^2)	$E_{c,L}$ (N/mm^2)	$G_{R,T}$ (N/mm^2)	$G_{R,L}$ (N/mm^2)	$G_{T,L}$ (N/mm^2)	$\mu_{R,T}$	$\mu_{R,L}$	$\mu_{T,L}$
	1018	572	12520	234	617	1321	0.683	0.022	0.048
Strength properties	$f_{c,R}$ (N/mm^2)	$f_{c,T}$ (N/mm^2)	$f_{c,L}$ (N/mm^2)	$\tau_{R,T}$ (N/mm^2)	$\tau_{R,L}$ (N/mm^2)	$\tau_{T,L}$ (N/mm^2)			
	3.3	2.5	27.5	20.6	9.3	9.3			

Note: $E_{c,R}$, $E_{c,T}$, $E_{c,L}$ are radial, tangential, longitudinal compression elasticity modulus respectively. $f_{c,R}$, $f_{c,T}$, $f_{c,L}$ are radial, tangential, longitudinal compression strength respectively. $G_{R,T}$, $G_{R,L}$, $G_{T,L}$ are shear modulus of transverse section, radial section, tangential section respectively. $\tau_{R,T}$, $\tau_{R,L}$, $\tau_{T,L}$ are shear strength of transverse section, radial section, tangential section respectively. $\mu_{R,T}$, $\mu_{R,L}$, $\mu_{T,L}$ are Poisson's ratio.

The timber material was fir which was widely used in ancient timber structures. The density of the timber material was 0.39g/mm^3, and the moisture content was about 12%. Timber is naturally an orthotropic material, and its mechanical properties are normally

measured in three directions, namely radial, tangential (circumferential) and longitudinal. The Young's modulus, shear modulus and Poisson's ratios of the timber material in the three directions were determined from standard timber material tests and the results are summarised in Table 1.

2.2 Test setup and loading scheme

The test setup is schematically shown in Figure 3. The column was pin-supported at the bottom end and loaded with a hydraulic jack from the top to maintain a desired axial force. A pair of roller supports was provided near the column top to prevent side movement. A vertical load was applied at the beam end which in turn exerted a bending moment, along with a shear force, at the test joint. The axial force in the column was 20kN which was decided according to relevant guide [16] and taking into account the reduced scale.

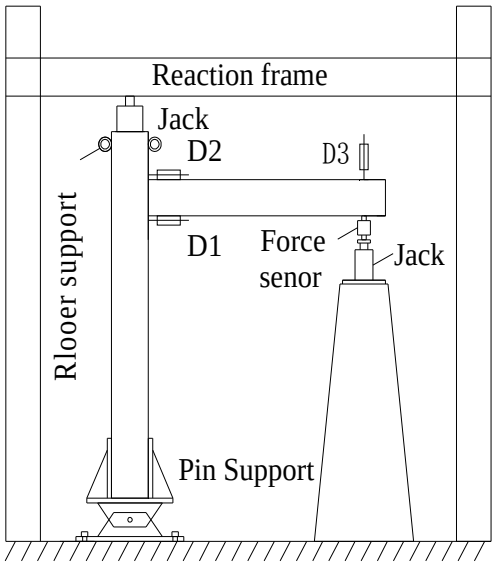

Figure 3 Schematic of the test setup

Three displacement transducers (LVDTs), numbered D1, D2 and D3 respectively, were arranged to measure the vertical displacement at the beam end (D3) and the rotational displacements of the joint (D1 and D2), as illustrated in the figure. The loading process was controlled by the displacement measured by D3 and the specimens were subjected to monotonic loading until the failure of the joint, which typically involved the pull-out of the tenon from the mortise.

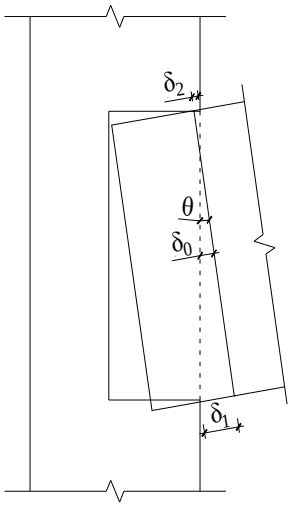

Figure 4 Characteristic deformations of the tenon relative to the mortise (beam-end deformations at the joint)

The overall deformations of the tenon relative to the mortise may be represented by a rotation (θ) and a pull-out displacement (δ_0). θ and δ_0 may be deduced from the relative displacements measured on the top and bottom of the beam, as:

$$\theta = (\delta_1 - \delta_2) / l_1 \tag{1}$$

$$\delta_0 = (\delta_1 + \delta_2) / 2 \tag{2}$$

where δ_1 and δ_2 are the readings from D1 and D2; for an upward load, δ_1 is positive and δ_2 is negative. l_1 is the vertical distance between D1 and D2.

The bending moment exerted on the dovetail joint (M) can be calculated as:

$$M = Pl_2 \tag{3}$$

where P is the vertical load applied at the beam tip (measured by a load cell), l_2 is the horizontal distance between the loading position and the right edge of the column.

2.3 General observations from the tests

Because of the jointing method in the dovetail joints, initial gaps of certain sizes always exist between the tenon and the mortise after installation. In the experiment these gaps were left untreated to represent an average condition in practice. In specimen JA-1, the apex gap was found to be 4.5mm and the top gap was 2mm before loading. The sizes of these gaps were 4.5mm and 3mm in specimen JA-2, and 5mm and 3mm in both JB-1 and JB-2. There was no side gap in both JA-1 and JA-2. The size of the side gaps was about 1mm in both JB-1 and JB-2 before loading.

The general observation from a typical test was as follows. Hiccup sound occurred

firstly with the squeezing and slipping movements between the tenon and the mortise. Then squeak sound occurred due to squashing of timber fibres as the rotation deformation increased. Figure 5(a) shows an overall deformation pattern. After that, the sounds intensified slowly while the overall response remained steady until the tenon pulled out, as shown in Figure 5(b). There was noticeable dent on the downside of the tenons apex and more pronounced dent on the upside of the tenon neck, as shown in Figure 5(c). The bottom of the mortise expanded slightly, as shown in Figure 5(d). The beam and column members remained in a good condition in all cases.

(a) Rotation (b) Pull-out (c) Fracture at tenon neck (d) Mortise

Figure 5 Failure modes of specimens JA-1 and JA-2

(a) Rotation (b) Pull-out c) Pressing damage on tenon apex (d) Mortise

Figure 6 Failure modes of JB-1 and JB-2

The general phenomenon during loading of Type-2 specimens was similar to that of JA-1 and JA-2, as shown in Figure 6. In JB-2, however, severe splitting cracks occurred in the column at the bottom of the mortise in the later loading stage leading to the detachment of D1, as shown in Figure 6(b).

2.4 Load – deformation relationships

Figure 7(a) shows the relationship between bending moment and rotation at the joint for all the four specimens. Specimens JA-1 and JA-2 had a similar pattern, although the initial stiffness and the maximum moment capacities exhibited some differences which may be attributed to the differences in the initial conditions (gap sizes) and variation in the wood material properties. The moment-rotation relationship did not have a clear elastic stage but the moment increased rapidly as the rotation increased until 50-60% of the peak load. This

was followed by a more gradual increase of the moment until reaching the peak due to plastic deformation in the material in the vicinity of the joint interfaces. In the post-peak stage the moment decreased gradually with the increase of rotation due to the pull-out of the tenon, showing good ductility.

In specimens JB-1 and JB-2 (joints below the column top), the moment-rotation relationship showed an initial settling stage, but as one can imagine the extent of this stage could vary with the workmanship. Ignoring the initial settling stage, the overall curves were similar to those of JA-1 and JA-2, except that the peak moments were markedly lower. The reduced moment capacities are believed to be mainly due to the effect of side gap.

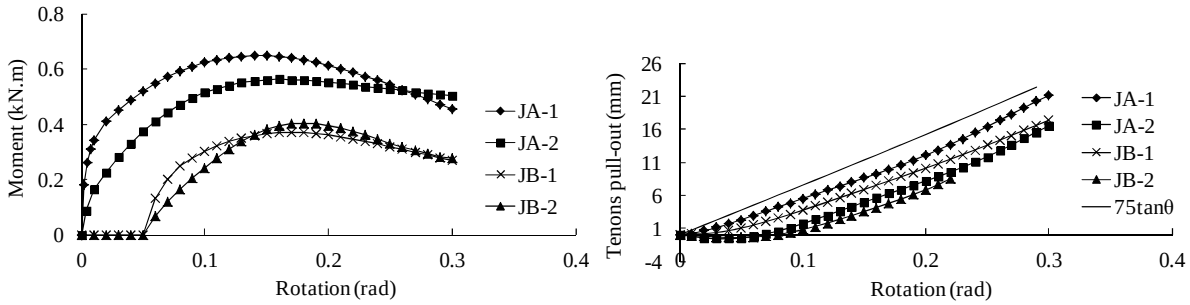

(a) Relationships of moment vs. rotation (b) Relationships of tenon pull-out vs. rotation

Figure 7 Flexural behaviours of joints under monotonic load

Figure 7(b) shows the tenon pull-out as a function of the rotation. An idealised relationship of $75\tan\theta$ (to be explained later in the next paragraph) is also included. Because of the effect of pre-existing gaps, the measured results in the early stage of loading did not exhibit a consistent relationship, but after a certain settlement stage, the relationship tended to follow the slope as expressed by the idealised curve. It is noted that because of the damage at the bottom of the mortise in specimen JB-2, the rotation measurement in the last part of the curve for JB-2 is not included.

The idealised relationship assumes no initial gap at the tenon top and that the centre of rotation is located at the top of the tenon neck section. The observed dent damage on the upside of the tenon neck in all specimens tends to support this assumption, barring the initial gap. Subsequently, the relationship between the tenon pull-out displacement δ_0, the height of tenons h and the rotation θ can be worked out easily by geometry, thus $\delta_0=0.5h\tan\theta$, where h is 150mm for all the four specimens.

3 Numerical simulation

Numerical simulation has been increasingly used to analyse the behaviour of timber structures / joints [17-18]. In the present study, finite element analysis has been conducted using ABAQUS software [19] to examine the deformation states and the stress distributions in the tenon and mortise of the joints. This information has been used to supplement the experimental observations to support the development of the theoretical model. To simplify the modelling analysis, complexities in the geometric imperfections were not considered in the finite element model. The specimen chosen for the modelling was JA-1 which had the smallest gaps among all four specimens. Based on the measurement from the experiment, the size of the gap to the top surface of the tenon was given 2mm in the finite element model.

3.1 Finite element model

The FE model has been developed using ABAQUS/Standard and the element type is C3D8R. Considering both the accuracy and the computational cost, the final mesh size was chosen to be 10mm for the tenon and mortise, and 20mm for the beam and column. Figure 8(a) shows the finite element mesh.

The basic constitutive model for timber is elasto-brittle in tension, and elasto-plastic in compression. The modulus of elasticity and the strength were made the same for both tension and compression, as shown in Figure 8(b).

Timber was modelled as an orthotropic material, and the nine mutually independent elastic constants and six strength values were given the measured material properties as shown in Table 1. Yielding was made to follow Hill yield criterion, which is suitable for orthotropic material and the yield surface is an elliptic cylinder.

The interaction between the tenon and the mortise was modelled as “hard contact” in the normal direction and “static-kinetic exponential decay” in the tangential direction. This means the interfaces can transfer pressure and tangential (friction) force but not tension. When the tangential force is smaller than the critical force f_s expressed in Equation (4), the two sides of the interface stick together. When the tangential force exceeds f_s, relative sliding would occur between the two sides of the interface, and a friction incurred in the process of sliding. The friction coefficient was assumed to decay with the sliding speed as expressed in Equation (5).

$$f_s = \mu_s N \tag{4}$$

$$\mu = \mu_k + (\mu_s - \mu_k) e^{-d_e \gamma_{eq}} \tag{5}$$

In the above equations, μ_s and μ_k are the static and dynamic friction coefficient, respectively. d_c is a decay coefficient of the friction coefficient, and γ_{eq} is the relative sliding speed between the tenon and the mortise. Assuming $\mu_s = 0.33$, $\mu_k = 0.26$ and $d_c = 3$ according to relevant literature [20-21], the friction coefficient μ can be obtained as a function of γ_{eq} as shown in Figure 8(c).

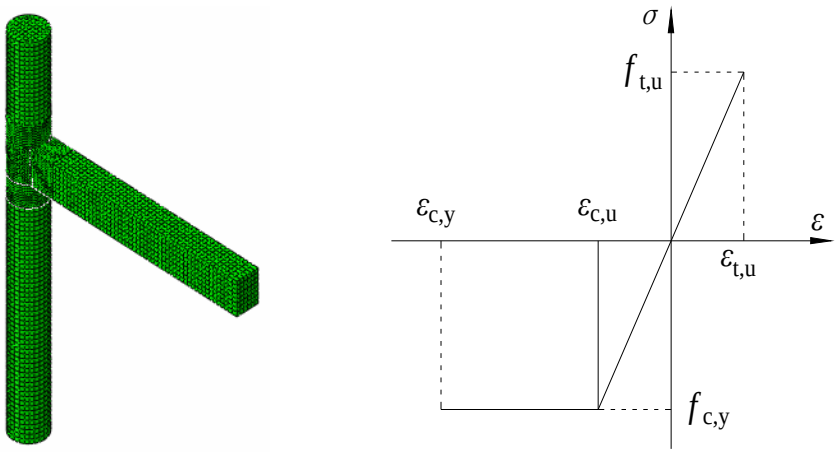

(a) FE mesh (b) Stress-strain relationship

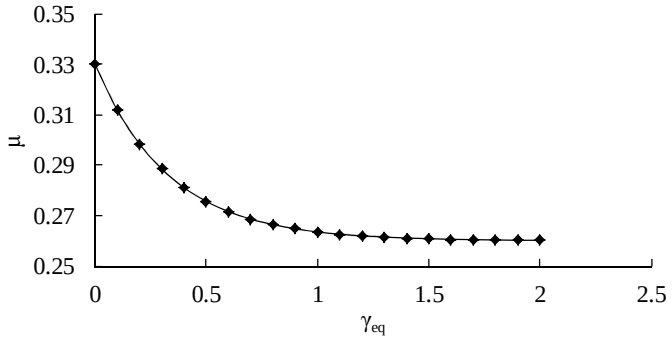

(c) Exponential decay friction model

Figure 8 FE model and material descriptions

3.2 Simulation results

The computed moment-rotation relationship using the FE model is compared with the experimental curve in Figure 9. The comparison shows a reasonably good agreement in terms of the overall trend, the peak moment, and the post-peak plastic deformation. Some discrepancies exist in the initial stiffness and the detail of pre-peak nonlinear response, but considering the complex interface actions and sliding movement, the FE simulation is can be regarded as satisfactory.

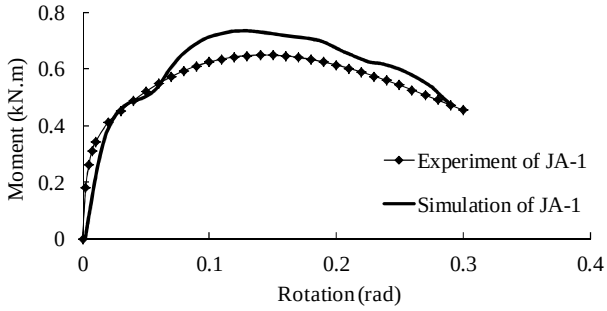

Figure 9 Comparison of moment-rotation relationships between FE and experimental results

The deformation of the joint and the distributions of stress within the tenon and the mortise region are shown in Figure 10. From Figure 10(a) it can be seen that the failure mode of the dovetail joint in the FE model is due to the pull-out of the tenon, which echoes the experimental observation. The FE model also captures the slight expansion deformation in the lower part of the mortise as the tenon is pulled out from there, as shown in Figure 10(b). The stress distribution within the tenon shown in Figure 10(c) indicates that high stresses develop in the upper part of the tenon apex, causing compressive deformation (dent) while the top side of the tenon neck experiences also higher stresses. All of these simulated phenomena agree well with the respective experimental observations.

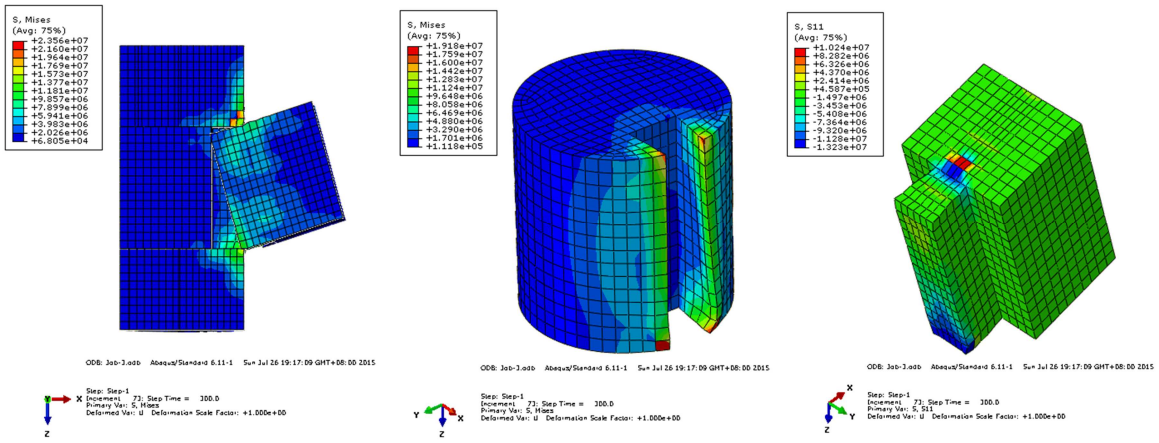

(a) Deformation (b) Mortise (c) Tenon

Figure 10 Deformation and stress contours at onset of tenon pull-out from FE analysis

The profile of the pressure on the two side faces of the tenon reflects how the joint behaves and will form an important assumption in the simplified theoretical model described later. Figure 11 shows the distributions of the normal pressure on the side faces over the height of the tenon near the apex and along the length of the tenon at the bottom level. It can be seen that compressive stress on the side faces of the tenon decreases with increase of the

distance from the bottom (in elevation) and from the apex (in plan). The distributions along both directions may be treated as approximately triangular.

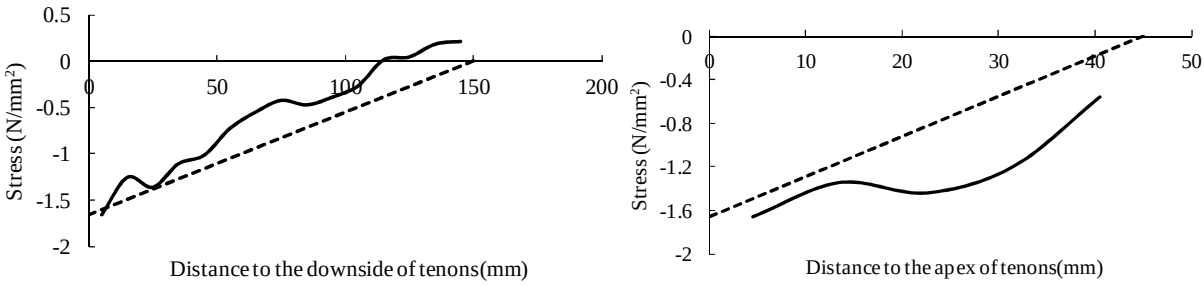

(a) Along the height of tenon (b) Along the length of tenon

Figure 11 Distributions of normal stress (pressure) on two side faces of tenon

3.3 Effect of dovetail slope

The width of the tenon apex is wider than that of the tenon neck, and the difference in the width gives rise to the dovetail slope. A comparison of the effect with and without the slope was made using the finite element model. The case with a typical slope was the same as in the test specimens shown in Figure 2(a), whereas the case without a slope had a uniform tenon width equal to 40mm (average of the dovetail tenon width). Figure 12 shows a comparison of moment-rotation relationship between the two joint cases.

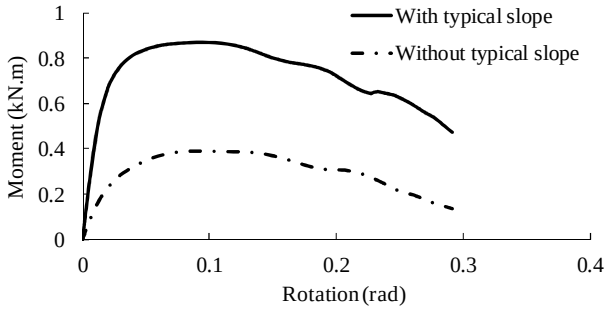

Figure 12 Effect of dovetail slope

It can be clearly observed that the case with a typical slope (dovetail tenon) has a considerably higher moment resistance than the case without a slope (flat tenon), due to much enhanced pressure and friction on the two side faces of the dovetail tenon as compared to the flat tenon.

4 Theoretical analysis

4.1 Basic assumptions

In this section we derive a simplified analytical model for the calculation of the moment-rotation relationship of general dovetail mortise-tenon joints.

A few basic assumptions are adopted, as follows:

(1) The bending deformation of the tenon itself is neglected. That is to say, the tenon only has a rigid motion within the mortise, thus the global displacement of every point in the tenon can be related to the rotation θ and the pull-out displacement δ_0 (refer to Figure 4).

(2) When extrusion occurs between longitudinal and transverse timber areas, the deformation takes place only in the transverse timber area.

(3) As the interaction on the two side interfaces between the tenon and the mortise are both under compression in the timber transverse direction, the compression deformation of the tenon is equal to the expanding deformation of the mortise at the same position.

4.2 Geometric conditions

The dimensions and geometric conditions before and after the deformation of a dovetail joint are depicted in Figure 13.

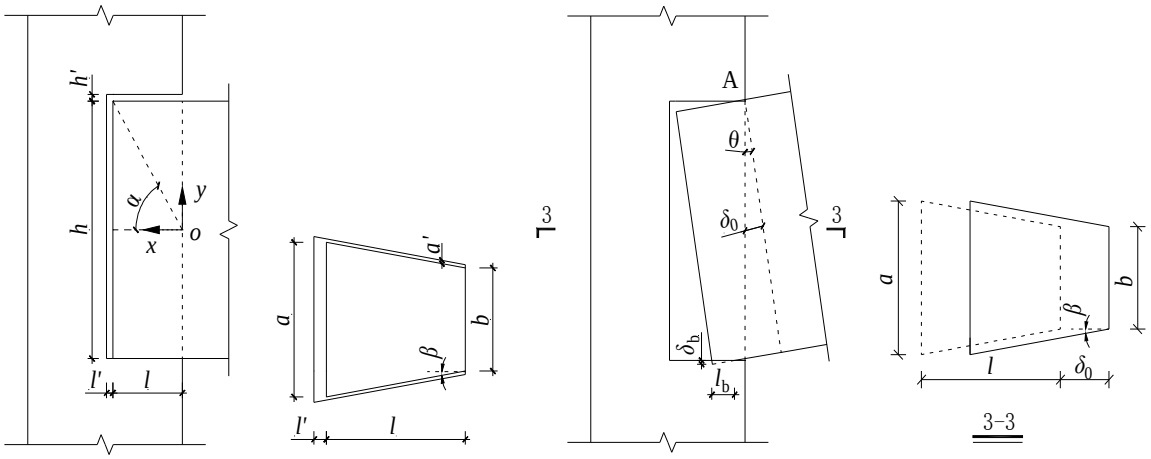

(a) Before deformation (original) (b) With deformation

Figure 13 Geometric conditions of dovetail joint

The length and height of the tenon are denoted as l and h respectively, and the width of the tenon apex and tenon neck are denoted as a and b respectively. The gaps at the apex, top and sides of the tenon are denoted as l', a' and h' respectively. Because the beam will shoulder any inward movement at the top of the tenon neck (refer to Figure 1), the tenon will

effectively rotate about a fixed point "A" in Figure 13(b), and so the tenon apex face (end face) will hardly come into contact with the mortise, rendering the apex face to be effectively free of stress. Define the two angles α and β, as shown in Figure 13(a). The subscripts "b", "t" and "s" denote bottom, top and side faces of the tenon, respectively.

The intersection between the tenon neck and the beam centreline is defined as the origin the x-y system (point "*o*" in Figure 13(a)). The positive direction of the x-axis (horizontal) is leftward and the positive direction of the y-axis (vertical) is upward. The compression deformation and the length of interface can be obtained by the geometric conditions.

As mentioned before, the relationship between the tenon pull-out δ_0, height h and rotation θ can be expressed as:

$$\delta_0 = 0.5h\theta \tag{6}$$

The maximum vertical compression deformation at the bottom of the tenon can be expressed as:

$$\delta_{\mathrm{b}} = l\sin(\alpha+\theta)/\cos\alpha - 0.5h - \delta_0\sin\theta - h' \tag{7}$$

The length of the contact area at the bottom of the tenon can be written as:

$$l_{\mathrm{b}} = \delta_{\mathrm{b}}\cos\theta \tag{8}$$

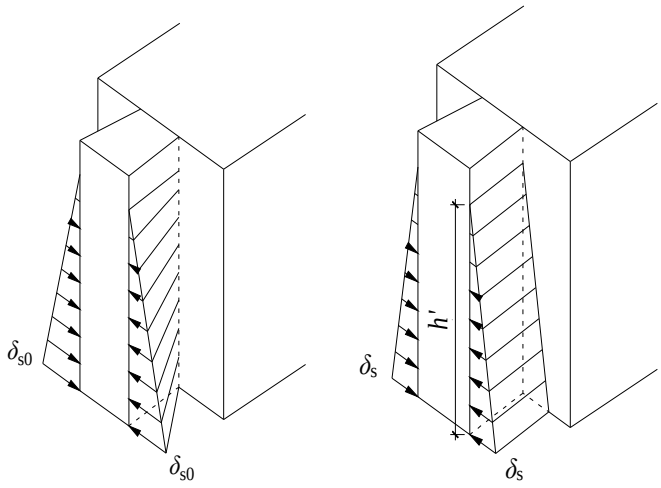

(a) Idealised (b) Simplified

Figure 14 Compressive deformation of the two side faces of the tenon

The compressive deformation states of the two side faces of the tenon can be established by consulting the results from the FE analysis shown in Figure 11. These may be idealised by a linear variation both in the elevation and plan views, as shown in Figure 14(a). Based on the geometry, the governing compression deformation at the bottom of the tenon apex can be expressed as:

$$\delta_{s0} = \{[l - l\cos(\alpha+\theta)/\cos\alpha + \delta_0\cos\theta]\tan\beta - a'\}/2 \tag{9}$$

In order to simplify the calculation, the compression deformation is further approximated with a uniform distribution along the tenon length as shown in Figure 14(b). Thus the side compression deformation at the bottom position, δ_s, becomes:

$$\delta_s = \{[l - l\cos(\alpha+\theta)/\cos\alpha + \delta_0\cos\theta]\tan\beta - a'\}/4 \tag{10}$$

Taking into account the side gap a′, the height of the side contact area can be obtained as:

$$h' = 4\delta_s h/(4\delta_s + a') \tag{11}$$

4.3 Equilibrium conditions

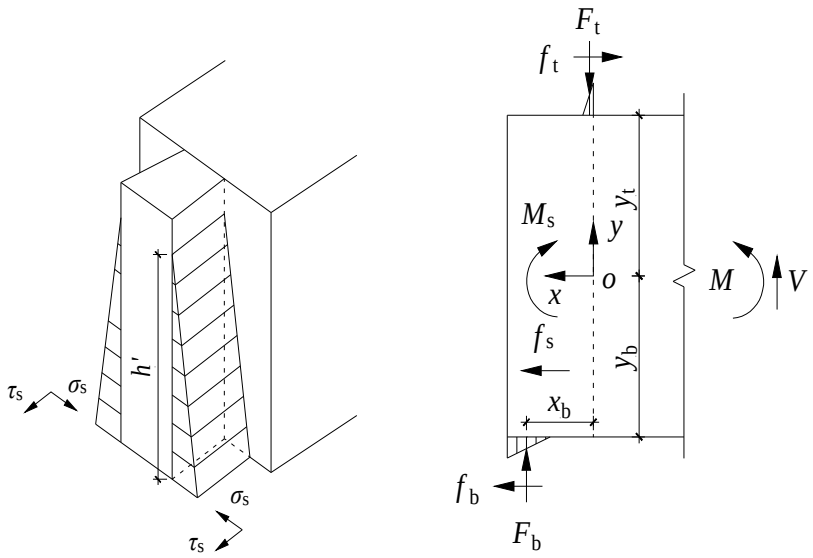

(a) Stress distribution on two side faces (b) Overall diagram of forces

Figure 15 Force diagram of the tenon in the elastic stage

Figure 15 illustrates the distribution of the normal and friction stresses on the side faces in the elastic stage, and the overall diagram of forces acting on the tenon of the dovetail joint. F_b and F_t represent the compression (normal) force on the bottom and top face of the tenon, respectively. F_t is located at point "A", which is the centre of rotation as mentioned before, and F_b is located at the centroid of bottom normal stress block. f_b is the friction corresponding to F_b, and f_t represents the friction corresponding to F_t as well as the mechanical locking force produced by the beam shoulder at the tenon neck. The horizontal distance from F_t to point *o* is very small, so the moment produced by F_t about "*o*" can be ignored. The friction stress on the two side faces is expressed as τ_s and their resultant is denoted as f_s. The moment produced by f_s about point *o* is M_s.

f_t can be obtained by the equilibrium of the horizontal forces:

$$f_t = f_b + f_s \tag{12}$$

Taking moment about "*o*", the total moment in the elastic stage produced by all components of the forces exerted on the tenon (which would be equal to the bending moment acting on the joint from the beam) can be obtained as.

$$M = F_b x_b + f_b y_b + f_t y_t + M_s \tag{13}$$

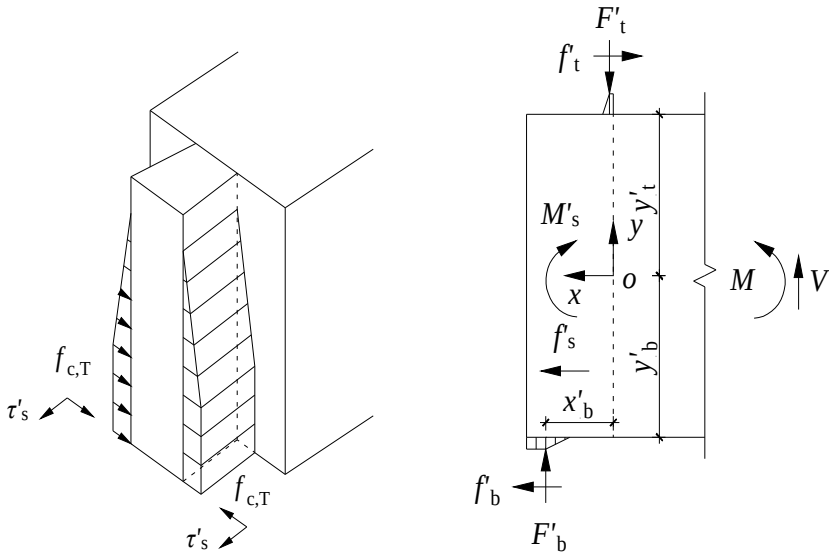

(a) Stress distribution on two side faces (b) Overall diagram of forces

Figure 16 Force diagram of the tenon in the elastoplastic stage

When the stressed areas of timber enter into elastoplastic stage, the stress patterns change from a triangle to a trapezoid, as shown in Figure 16. Replacing F_b, f_b, f_t, f_s, τ_s, M_s, x_b, y_b, y_t with F'_b, f'_b, f'_t, f'_s, τ'_s, M'_s, x'_b, y'_b, y'_t, equations (12) and (13) still apply.

4.4 Physical conditions

4.4.1 Elastic stage

The normal stress acting on the bottom face of the tenon may be related to the normal (vertical) compressive strain, which is in turn related to the vertical deformation. Approximating the vertical strain at the tenon apex along the height as linear, we can relate the governing vertical compressive strain ε_b to the vertical deformation δ_b as:

$$\delta_b = 0.5 \times h \times \varepsilon_b = 0.5 h \varepsilon_b \tag{14}$$

Therefore the maximum compressive stress at the bottom level of the tenon is:

$$\sigma_b = E_{c,R} \varepsilon_b = 2 E_{c,R} \delta_b / h \tag{15}$$

Note that the timber material property parameters follow the definitions given in Section

2.1 and Table 1.

The resultant forces on the bottom face of the tenon are therefore:

$$F_{\mathrm{b}} = 0.5 a l_{\mathrm{b}} \sigma_{\mathrm{b}} \tag{16}$$

$$f_{\mathrm{b}} = \mu F_{\mathrm{b}} \tag{17}$$

The lever arms of the respective forces with respect to point "*o*":

$$x_{\mathrm{b}} = l - l_{\mathrm{b}} / 3 \tag{18}$$

$$y_{\mathrm{b}} = y_{\mathrm{t}} = 0.5h \tag{19}$$

The maximum normal and shear (friction) stresses over the two side faces can be expressed as follows:

$$\sigma_{\mathrm{s}} = \varepsilon_{\mathrm{s}} E_{\mathrm{c,T}} = \frac{2\delta_{\mathrm{s}}}{0.5(a+b)} E_{\mathrm{c,T}} = 4E_{\mathrm{c,T}} \delta_{\mathrm{s}} / (a+b) \tag{20}$$

$$\tau_{\mathrm{s}} = \mu \sigma_{\mathrm{s}} \tag{21}$$

The distribution of the friction over the two side faces in the elastic stage is shown in Figure 17(a). Accordingly the horizontal resultant force is:

$$f_{\mathrm{s}} = 2 \times 0.5 \times \tau_{\mathrm{s}} \times h' \times (l - \delta_0) = \tau_{\mathrm{s}} h' (l - \delta_0) \tag{22}$$

The resisting moment produced by f_{s} about point "*o*" can be expressed as:

$$M_{\mathrm{s}} = \tau_{\mathrm{s}} h' (l - \delta_0) \times (h/2 - h'/3) = \tau_{\mathrm{s}} h' (h/2 - h'/3)(l - \delta_0) \tag{23}$$

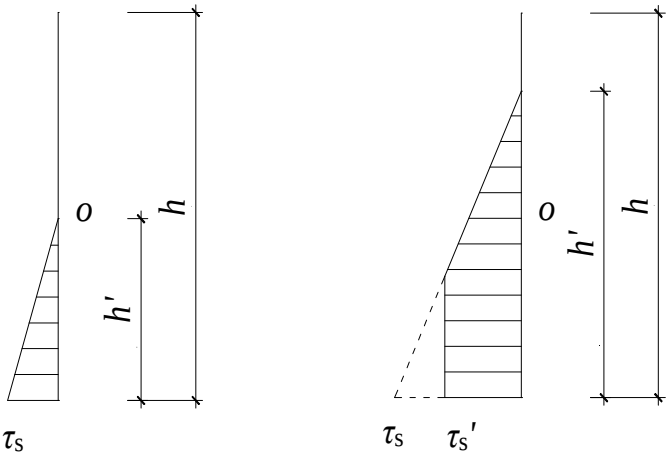

(a) Elastic stage (b) Elastoplastic stage

Figure 17 Distribution of friction on side faces along the height of tenon

4.4.2 Elastoplastic stage

The respective stresses and forces can be expressed as follows:

$$F_{\mathrm{b}}' = [1 - (1 - \frac{f_{\mathrm{c,R}} h}{2E_{\mathrm{c,R}} \delta_{\mathrm{b}}})] F_{\mathrm{b}} \tag{24}$$

$$f_{\mathrm{b}}' = \mu F_{\mathrm{b}}' \tag{25}$$

$$\tau_{\mathrm{s}}' = \mu f_{\mathrm{c,T}} \tag{26}$$

The lever arms of the forces are respectively:

$$x_{\mathrm{b}}' = l - \frac{(\delta_{\mathrm{b}} - f_{\mathrm{c,R}} h / 4E_{\mathrm{c,R}})^2 + {f_{\mathrm{c,R}}}^2 h^2 / 48{E_{\mathrm{c,R}}}^2}{(2\delta_{\mathrm{b}} - f_{\mathrm{c,R}} h / 2E_{\mathrm{c,R}})\delta_{\mathrm{b}} / l_{\mathrm{b}}} \tag{27}$$

$$y_{\mathrm{b}}' = y_{\mathrm{t}}' = 0.5h \tag{28}$$

The distributions of the friction over the two side faces in the elastoplastic stage are shown in Figure 17(b). The horizontal resultant force can be expressed as:

$$f_{\mathrm{s}}' = (2\tau_{\mathrm{s}} - \tau_{\mathrm{s}}')\tau_{\mathrm{s}}' h'(l - \delta_0) / \tau_{\mathrm{s}} \tag{29}$$

The resisting moment produced by f'_{s} about point *o* can be obtained as:

$$M_{\mathrm{s}}' = h'(l - \delta_0)\{\tau_{\mathrm{s}}(\frac{h}{2} - \frac{h'}{3}) - \frac{(\tau_{\mathrm{s}} - \tau_{\mathrm{s}}')^2[\frac{h}{2} - \frac{(\tau_{\mathrm{s}} - \tau_{\mathrm{s}}')h'}{3\tau_{\mathrm{s}}}]}{\tau_{\mathrm{s}}}\} \tag{30}$$

4.5 Simplified calculation procedure

With the complete formulation presented in Section 4.4, the detailed moment-rotation relationship of a dovetail joint can already be calculated; however, it will require a significant amount of calculation. Considering that the generation of the complete curve may not always be necessary in actual applications, a simplified calculation procedure for the determination of the key points of the moment-rotation relationship can be very useful and this is presented in what follows.

4.5.1 Simplified formulation

Four characteristic points are of interest to practical applications, namely:

(1) The settling point when the moment begins to develop, with an initial rotation θ_{i} and a zero moment ($M_{\mathrm{i}} = 0$).

(2) The initial yield point when the timber material at the two side faces begins to enter into plastic range, with a rotation θ_{y} and a moment M_{y}.

(3) The maximum (peak) moment, M_{p}, and the corresponding rotation, θ_{p}.

(4) The failure or ultimate point when the tenon is at the onset of pull-out from the mortise, with a rotation θ_{u} and a moment M_{u}.

For relatively small θ (as in general applications), $\cos\theta \cong 1 - \theta^2$, $\sin\theta \cong \theta$, $\tan\theta \cong \theta$. The compression stress patterns are further simplified from a trapezoid to a rectangular shape, and

the higher order terms involving θ which have litter effect on the result are ignored. Simplified formulas are thus obtained for the above mentioned characteristic points, as detailed below.

a) The initiation point

Let the rotation required to settle the top and side gaps of the tenon be θ_1 and θ_2, respectively. The initiation rotation is therefore:

$$\theta_{\mathrm{i}} = \min\{\theta_1, \theta_2\} \tag{31}$$

θ_1 can be obtained by making δ_{t} in Equation (7) equal to 0:

$$\theta_1 = \frac{2(l - \sqrt{l^2 - 3hh'})}{3h} \tag{32}$$

θ_2 can be obtained by making δ_{s} in Equation (10) equal to 0:

$$\theta_2 = \frac{-h + \sqrt{h^2 + 2la'\cot\beta})}{l} \tag{33}$$

b) Initial yield point

The initial yield rotation can be obtained by making σ_{s} in Equation (20) equal to $f_{\mathrm{c,T}}$:

$$\theta_{\mathrm{y}} = \frac{-h + \sqrt{h^2 + 2l[a' + \frac{(a+b)f_{\mathrm{c,T}}}{E_{\mathrm{c,T}}}]\cot\beta}}{l} \tag{34}$$

The yield moment can be obtained by substituting Equation (34) into (13):

$$M_{\mathrm{y}} = \frac{4\mu E_{\mathrm{c,T}}(l - 0.5h\theta_{\mathrm{y}})h^2 k_1}{a+b} \frac{4k_1}{4k_1 + a'}[1 - \frac{4k_1}{3(4k_1 + a')}] \tag{35}$$

where

$$k_1 = [(0.5l\theta^2 + h\theta)\tan\beta - a']/4 \tag{36}$$

c) Peak point

The peak rotation can be obtained by rearranging Equation (13) to get θ:

$$\theta_{\mathrm{p}} = \sqrt{\frac{(a+b)f_{\mathrm{c,T}}l}{E_{\mathrm{c,T}}\tan\beta h^2}} + \theta_1 + \theta_2 - \theta_{\mathrm{i}} \tag{37}$$

where θ_{i}, θ_1 and θ_2 are determined from equations(31), (32)and(33).

The peak moment can be obtained by substituting Equation (37) into (13):

$$M_{\mathrm{p}} = af_{\mathrm{c,R}}k_2(l - 0.5k_2 + \mu h) + \mu f_{\mathrm{c,T}}(l - 0.5h\theta_{\mathrm{p}})\frac{4k_1h^2}{4k_1 + a'} \tag{38}$$

where k_1 is defined in Equation (36) and k_2 is expressed as:

$$k_2 = -0.75h\theta_p + l - \frac{h'}{\theta_p} \tag{39}$$

d) Failure point

The tenon is at the onset of pull-out from the mortise when δ_0 reaches $0.5l$ (refer to Figure 1). The failure rotation can therefore be determined by:

$$\theta_u = \arctan l / h \tag{40}$$

The failure moment can be deteremined by substituting Equation (40) into (13):

$$M_u = \mu f_{c,T} l h^2 \frac{2k_1}{4k_1 + a'} \tag{41}$$

4.5.2 Verification of simplified calculations

The verification of the above simplified calculation procedure is firstly carried out on the experiments described in Section 2. The value of friction coefficient μ is 0.26. The dimensions and material properties of the specimens are assumed in accordance with the actual values shown in Figure 2 and Table 1. The sizes of the gaps also follow the measured values; h' is 2mm and 3mm for the traditional and modified dovetail joints, respectively, a' is 0mm and 1mm for the traditional and modified dovetail joints, respectively.

The four key points can be calculated by substituting the relevant parameters into the simplified formulas (31)-(41), and the results are shown in Figure 18 with comparison to the experimental curves. It can be seen that the results from the simplified mechanical model are consistent with the experimental data; the peak strength, peak deformation, as well as the stiffness in the first stage of the response, all agree well with the experimental results. The differences in the detailed response may be attributed primarily to the measuring errors of the gaps.

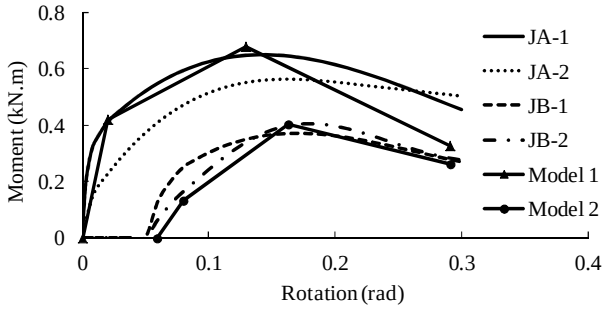

Figure 18 Comparison between the predicted moment-rotation relationship using the simplified mechanical model and the experimental results

Figure 18 also indicates that the moment-rotation relationship may be simplified into a

trilinear model consisting of an elastic segment, a plastic segment and a descending segment. There will be an initial settlement stage (horizontal line at zero moment) prior to the trilinear model if gaps are present around the tenon.

Further verification of the simplified mechanical model is carried out with respect to the experiments reported by Xu et al. [13]. The specimens in the above paper were dovetail joints, and the transverse compressive strength and modulus of elasticity of the timber material were 3MPa and 872MPa, respectively. Other parameters from the experiments included: l = 50mm, h = 150mm, a = 50mm, b = 40mm, h'=1mm. No information was available about the size of the side gaps, and this is assumed to be 0.5mm on the basis of the average gap size from the present study. The comparisons between the predictions using the simplified mechanical model and the experimental results are shown in Figure 19. It should be noted that the original experiments were under cyclic loading and the results being compared here are the envelope curves. It can be observed again that the simplified mechanical model produces a reasonable prediction as compared with the experimental results.

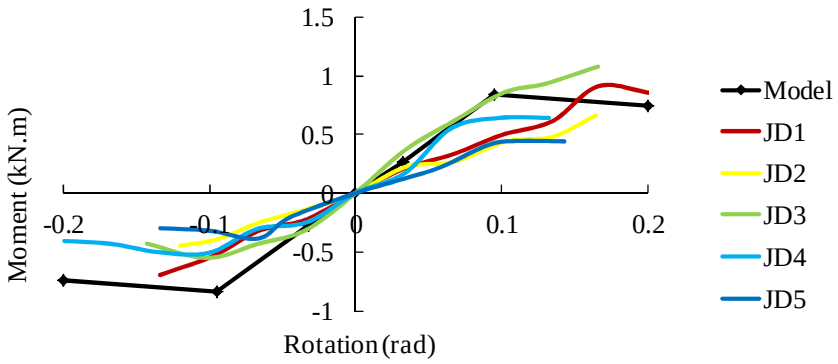

Figure 19 Further verification of the simplified mechanical model

5 Conclusions

This paper presents a comprehensive study on the behaviour of the timber dovetail joints by means of both experimental and numerical investigations. A theoretical model for the dovetail joints is also developed with the support from the experimental and numerical results. Finally a simplified calculation procedure is proposed for the determination of characteristic points on the moment-rotation relationship, from which a piece-wise linear moment-rotation curve can be established for the design analysis of timber structures involving dovetail joints. More specific conclusions from the experimental and numerical studies include:

(1) The main failure mode of the dovetail joints from the current experiments has been

the pull-out of the tenon. In this process, local pressing damage (dent) to the tenon and apparent expansion of the mortise have been observed. The beam and column members have been found to remain intact, and this indicates that the joint has been the weak link in the beam-column assemblies.

(2) The gaps within the joint have a great influence on the flexural behaviour, as can be expected. Relatively speaking, the side gaps have been found to affect more significantly than the top gaps, whereas the gaps on the apex have had the least effect. Such influences of the gaps are believed to be an important feature of the dovetail joints, and they reflect the significant role of the interface through the two dovetail sides of the tenon in the major deformation process.

(3) Both experimental and FE analysis results have shown that the moment-rotation relationship of the joints has an initial stage of gradual development of nonlinearity, followed by a prolonged yielding phase, and then a descending branch. As such, the moment-rotation relationship may be simplified into a trilinear model consisting of an elastic segment, a plastic segment and a descending segment.

(4) The simplified version of the theoretical model captures well the characteristic states, and thereby the key points, in the moment-rotation relationship for the dovetail joints. The model can also predict the initial settlement stage when gaps are involved in the joints.

Due to the uncertainties involved in the construction of the dovetail joints, particularly the size of the gaps within the joint region, further work is required to establish the statistical features of the moment-rotation relationship due to such uncertainties.

Acknowledgments

This work was financially supported by the Twelfth Five-Year national science and technology support program (2012BAJ14B02) and the Ph.D. Candidate Research Innovation Fund of Southeast University, Ministry of Education, China (CXLX13_101).

References

[1] Else G. The Yingzao-Fashi, its time and editor. International Conference on Chinese Architectural History I. Beijing: Tsinghua University Press; 1998.

[2] Liang S. Construction technology of Chinese ancient timber structures. Beijing: Tsinghua University Press; 2006.

[3] Yeomans DT. The Repair of Historic Timber Structures. Thomas Telford Publishing,

London; 2003.

[4] Ma B. Construction technology of Chinese ancient timber structures. Beijing: Science Press; 2003. (in Chinese)

[5] Chang WS, Hsu MF, Komatsu K. Rotational performance of traditional Nuki joints with gap I: theory and verification. Journal of Wood Science 2006; 52(1): 58-62.

[6] Chang WS, Hsu MF. Rotational performance of traditional Nuki joints with gap II: the behavior of butted Nuki joint and its comparison with continuous Nuki joint. Journal of Wood Science 2007; 53(1): 401-407.

[7] King WS, Yen JYR, Yen YNA. Joint characteristics of traditional Chinese wooden frames. Engineer Structures 1996; 18(8):635–644

[8] D'Ayala DF, Tsai PH. Seismic vulnerability of historic Dieh–Dou timber structures in Taiwan. Engineering Structures 2008; 30(8): 2101-2113.

[9] Chang WS, Hsu MF (2005) Mechanical characteristics of traditional Go-Dou and stepped dovetail timber connections in Taiwan (in Chinese). Taiwan Journal of Forest Science 2005; 20(1):61–71

[10] Qing C, Zhi Y, Pan J. Experimental study on seismic characteristics of typical mortise-tenon joints of Chinese southern traditional timber frame buildings. Science China technological science 2011; 54(9): 2404-2411.

[11] Yue Z. Traditional Chinese wood structure joints with an experiment considering regional differences. International Journal of Architectural Heritage 2014; 8(2): 224-246.

[12] Li Q. Study of rabbets and mechanical properties and seismic performance of timber frame of Chinese historic timber buildings. Xi'an: Xi'an University of Architecture and Technology; 2008. (in Chinese)

[13] Xu M. Study of aseismatic behaviour of mortise-tenon joints in Chinese ancient timber buildings. Nanjing: Southeast University; 2011. (in Chinese)

[14] Pang SJ, Oh JK, Park JS, et al. Moment-carrying capacity of dovetailed mortise and tenon joints with or without beam shoulder. J Struct Eng 2011; 137(7): 785-789.

[15] Seo JM, Choi IK, Lee JR. Static and cyclic behaviour of wooden frames with tension joints under lateral load. J Struct Eng 1999; 125(3): 344-349.

[16] Wang T. Static analysis of ancient timber structures. Beijing: Cultural Relics Press; 1992. (in Chinese)

[17] Sangree RH, Schafer BW. Experimental and numerical analysis of a halved and tabled traditional timber scarf joint. Construction and Building Materials 2009; 23: 615–624.

[18] Parisi MA, Cordié, C. Mechanical behavior of double-step timber joints. Construction

and Building Materials 2010; 24: 1364–1371.

[19] Hibbitt, Karlsson & Sorensen, Inc., Abaqus theory manual, version 6.11; 2006.

[20] Meng Q. The study for frictional properties of wooden materials and the impact on wood structure design. PhD thesis. Harbin: Northeast Forestry University; 2010. (in Chinese)

[21] Chen Z. Behaviour of typical joints and the structure of Yingxian wood pagoda. Harbin: Harbin Institute of Technology; 2011. (in Chinese)